6.3 CLUSTER DYNAMICS MODELING OF NANO-SCALE DEFECT AGGLOMERATION IN THIN MOLYBDENUM FOILS BENCHMARKED BY IN-SITU ION IRRADIATION UNDER TEM

— Donghua Xu and Brian D. Wirth (Department of Nuclear Engineering, University of Tennessee, Knoxville, TN 37996, USA)

OBJECTIVE

Irradiation effects on materials are generally initiated by the creation of atomic scale defects and their subsequent agglomeration into nano- and larger size clusters. The objective of this study is to enhance the understanding of the defect dynamics in early stage of irradiation in structural metals through combined modeling and experiments.

SUMMARY

In a recent coordinated effort, we have studied defect cluster dynamics in nanometer-thick molybdenum foils under 1 MeV Krypton ion irradiation at 80°C through both cluster dynamics computation and in-situ TEM experiments. By making direct one-to-one comparisons with experimentally observed cluster number density and size distribution as functions of foil thickness and irradiation dose and dose rate, significant validation and optimization of the model have been conducted in terms of both physical contents (damage production mode, identities of mobile defects) and parameterization (diffusivities of mobile defects). The optimized model exhibits excellent agreement with the current set of experiments both qualitatively and quantitatively, while further validation of the model and parameterization will continue to be pursued in the future with respect to Kr ion irradiation at varied temperatures and neutron irradiations on Mo.

PROGRESS AND STATUS

Introduction

In coordination with a recent set of in-situ TEM irradiation experiments we simulated the defect dynamics in nanometer-thick molybdenum foils under 1 MeV Krypton ion irradiation at 80°C using the cluster dynamics code, PARASPACE (PARAllel SPAtially-dependent Cluster Evolution), developed by our group previously. In this report, the experimental conditions and main experimental results will be summarized first, and then detailed model validation and optimization through drawing direct comparisons with experiments will be presented. Both physical contents (damage production mode, identities of mobile defects) and parameterization (diffusivities of mobile defects) of the model will be examined in detail. Further, surface effect and additional factors that are relevant to the model or the comparison of the model with the experiments will be addressed, such as dislocation sinking effect.

Summary of Experiments

In-situ Kr^+ ion irradiation was performed at 80°C and 1 MeV ion energy using IVEM-Tandem on TEM molybdenum foils thinned to perforation in the center with a peripheral thickness around 150 nm. Each foil was irradiated at a fixed ion flux and there were totally three different fluxes, 1.6×10^{11}, 1.6×10^{10} and 1.6×10^{9} ions/cm^2/s used for all the foils. The irradiation as well as

observation was performed up to a fluence of 1.5×10^{13} ions/cm^2 at the highest flux and 5×10^{12} ions/cm^2 at the two lower fluxes.

The damage production of 1 MeV Kr^+ in Mo was first calculated using SRIM-2008 with a displacement energy of 60 eV, assuming a Frenkel-pair production mode, which yielded an average production of 1.9 vacancies/ion/Å within the thickness range of the TEM foils. Then the nominal doses and dose rates corresponding to the above fluences and fluxes were evaluated based on the following equation:

$$\text{dose} = \frac{\Phi \times 10^8 \times \text{damage-production}}{N}, \tag{1}$$

where Φ is the fluence in ions/cm^2, the damage production is in vacancies/ion/Å obtained with SRIM, and

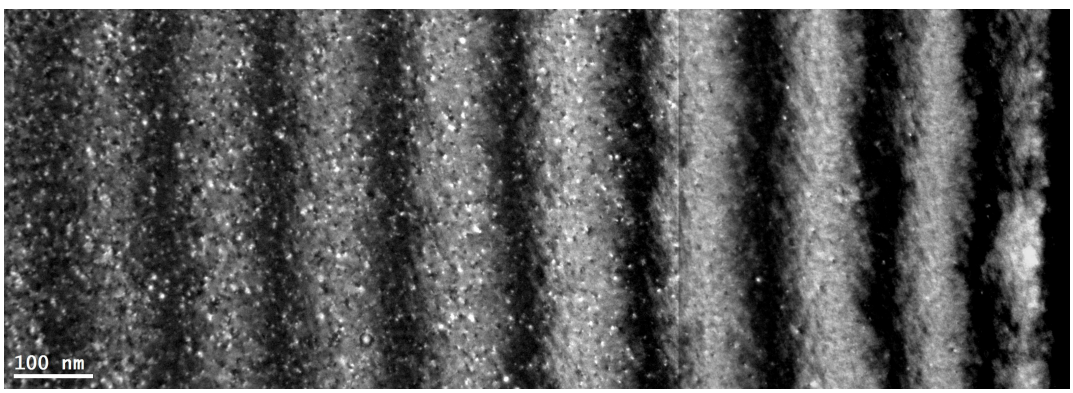

Figure 1. A composite of two plane-view dark-field micrographs showing defect structure distribution with increasing thickness (from right to left) in Mo in situ irradiated to 5×10^{12} ions/cm^2 at a flux of 1.6×10^{11} ions/cm^2/s and 80°C with 1 MeV Kr^+ ions.

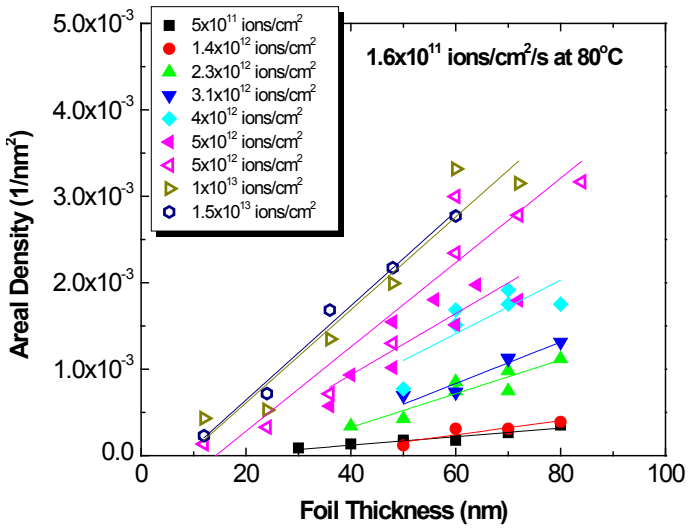

Figure 2. Areal density of defect clusters as a function of foil thickness and ion fluence in Mo in situ irradiated with 1 MeV Kr^+ ions at a flux of 1.6×10^{11} ions/cm^2/s at 80°C. Note that the solid symbols and the open symbols represent data from two different foils.

N is the atomic number density in atoms/cm^3. The nominal dose rates hence calculated are 5×10^{-4}, 5×10^{-5}, and 5×10^{-6} dpa/s, and the nominal finish doses are 0.045 dpa at the highest flux and 0.015 dpa at the two lower fluxes. As will be shown later, the assumed Frenkel-pair production mode is inadequate to satisfactorily reproduce the key experimental results, and intra-cascade cluster production has to be employed in the model in order to achieve good agreement with experiments. Hence, in the following text, ion fluences and fluxes rather than the doses and dose rates will be used in the comparisons between model and experiments.

During the in-situ irradiation of each foil at a selected flux, dark field (DF) micrographs (illustrated in Fig. 1) were taken at a series of selected fluences to record the defect (bright dots on the DF micrographs) evolution dynamics. Note that the fringes on a micrograph correspond to varying thicknesses (increasing from the foil center towards the foil periphery). From each DF micrograph, areal density and size distribution of defect clusters can be determined at different foil thicknesses, and overlaying such data from a series of micrographs taken from the same foil discloses the dose (fluence) dependence of the cluster evolution. Figure 2 provides such an example, showing the composite plot containing both thickness and fluence (dose) dependences of defect areal density for a foil irradiated at a flux of 1.6×10^{11} ions/cm^2/s to a fluence of 1.5×10^{13} ions/cm^2. Further, the dose rate dependence of defect evolution can be examined by comparing the above composite plots made for foils irradiated at different ion fluxes.

The defects observed are all dislocation loops and their Burgers vectors were analyzed. However, the defect character, interstitial- or vacancy-type, has yet to be determined, even though there is a reason to believe that the loops are of interstitial type.

Model Description

With 1D spatial dependence, the ODE (ordinary differential equation) system describing defect evolution changes to a PDE (partial differential equation) system, and the PDEs generally have the following generic form:

$$\frac{\partial C_i^{x_n}}{\partial t} = \varphi \times P_i(x_n) + D_i \frac{\partial^2 C_i^{x_n}}{\partial x^2} + GRT + GRE - ART - ARE \,, \tag{2}$$

where $C_i^{x_n}$ refers to the volumetric concentration (in 1/nm^3) of the *i*-th cluster at the depth position x_n (in nm), φ is ion flux (in ion/nm^2/sec), $P_i(x_n)$ is the production "probability" (in 1/ion/nm) of the *i*-th cluster by irradiation that is obtained through SRIM (combined with MD if not only Frenkel pairs are produced), D_i is the diffusivity of the *i*-th cluster, GRT is the rate of generation of the *i*-th cluster by trapping reactions ($A + B \rightarrow i$) among other clusters, GRE is the rate of generation of the *i*-th cluster by emission processes ($C \rightarrow i + B$) of other clusters, ART is the rate of annihilation of the *i*-th cluster by its trapping reaction with other clusters ($i + B \rightarrow C$), and ARE is the rate of annihilation of the *i*-th cluster by its own emission process ($i \rightarrow A + B$). The trapping (forward) and emission (backward) reaction constants are determined as follows (for a sample reaction $A + B \rightleftharpoons C$):

$$k^+ = 4\pi\left(r_A + r_B\right) \times \left(D_A + D_B\right), \tag{3}$$

and,

$$k^- = k^+ C_0 \exp\left(-\frac{E_b}{k_B T}\right), \tag{4}$$

where r_A and r_B are the trapping radii of clusters A and B typically taken as equivalent to the geometric radii of the clusters in the classical rate theory, D_A and D_B are the diffusivities, C_0 is the atomic number density of the matrix (here molybdenum) in 1/nm^3, and E_b is the binding energy of a single point defect to the cluster C (either A or B is a point defect or they both are). For trapping reactions among interstitials and/or interstitial clusters/loops k^+ and k^- are both scaled by a bias factor of 1.2. The diffusivity of a defect/cluster depends on the temperature according to Arrhenius law, i.e.,

$$D = D_0 \exp\left(-\frac{E_m}{k_B T}\right) \tag{5}$$

where D_0 is a prefactor and E_m is the migration energy. The monomer binding energy E_b is defined by the reduction in the summed formation energy (enthalpy, E_f) after binding occurs, for example, $E_b^{I_{10}} = E_f^I + E_f^{I_9} - E_f^{I_{10}}$. From Eqs. 2-5 it is evident that the diffusivities of various clusters, as determined by D_0 and E_m, play a very important role in the cluster evolution by affecting the trapping and emission kinetics within a certain depth grid as well as the diffusion kinetics across neighboring grids. The binding energies represent thermal stability of the clusters and determine (in combination with diffusivities) their emission rates, and their role in cluster evolution is limited at low temperature such as in the current study but may become significant at relatively high temperatures.

Initially, thermal equilibrium concentrations are set for point defects, i.e., single interstitial and single vacancy, and the concentrations of all other defects/clusters are set to zero at all depth

grids. Note that values of 3 eV and 7 eV were used for the formation energy of single vacancy and single interstitial in Mo, respectively, similar to those reported from experiments and/or ab initio calculations. These E_f values correspond to extremely small thermal equilibrium concentrations of point defects. During the entire PDE solving and time integration process, the concentrations of all defects/clusters except the point defects are maintained at zero on the two surfaces of the foil whereas the point defects are maintained at their thermal equilibrium on the surfaces. With this boundary condition, the foil surfaces are treated explicitly as black sinks and thus the surface sinking effect is directly accounted for without having to use empirical formulations.

RESULTS

In this section, model calculations based on different assumptions with respect to damage production mode (Frenkel pair mode or intracascade cluster production mode) and mobile clusters (number of mobile clusters and their mobilities) will be compared against each other and directly against experiments. It will be shown that the simple model assumptions lead to large deviation from experiments unless abnormal parameter values are used, whereas more sophisticated model assumptions are able to produce excellent agreement with key experimental results after reasonable small amount of parameter optimization.

Numerous previous studies, both computational and experimental, have suggested interstitial clusters (I_n) exist in the form of two-dimensional loops in irradiated BCC metals. Hence their sizes are determined as:

$$d = 2r = 2 \times \left(\frac{nV_a}{\pi b} \right)^{1/2}, \tag{6}$$

where d is the diameter, r is the radius, V_a is the atomic volume of Mo, and b is the Burgers vector length. The present experiments revealed two types of loops with Burgers vectors 1/2<111> and <100>, constituting an average of 77% and 23% of the total loop population, respectively. In the current modeling, we do not distinguish the two types of loops, and the Burgers vector length of 1/2<111> is used for all I_n clusters. Note that the diameter values corresponding to the two different Burgers vectors for a given n only differ by a factor of 1.07.

Vacancy clusters (V_n) have been frequently observed in previous studies as three-dimensional voids in BCC metals, in which case their sizes are determined as:

$$d = 2r = 2 \times \left(\frac{3nV_a}{4\pi} \right)^{1/3}. \tag{7}$$

Frenkel Pair Production Mode and Only Single Interstitial & Single Vacancy Mobile

Frenkel pair production is a simple damage mode in which equal numbers of single interstitials and single vacancies are produced by irradiation. While it is often considered a good depiction of electron irradiations, it may not be sufficient to fully describe ion irradiations, particularly when high-energy ions are involved. In this subsection and the next we first explore the possibility of reproducing the experiments with this simple production mode.

Resistivity recovery experiments have been performed previously to determine the migration energies of single interstitials and single vacancies in Mo. Interstitial migration energy E_m^I was reported to be 0.083 eV based on a 2nd order rate equation fit to the recovery stage at 33~39 K, and values ranging from 1.35 to 1.89 eV were reported for vacancy migration energy E_m^V based on the slope change in the recovery stage at 520 K with an assumed sink density. These values provide at least a good estimate, although their accuracy may be worthy of more experimental verification, particularly the vacancy migration energy which may depend on material purity and the assumptions used to analyze the recovery data at 520 K where various vacancy and interstitial clusters may co-exist.

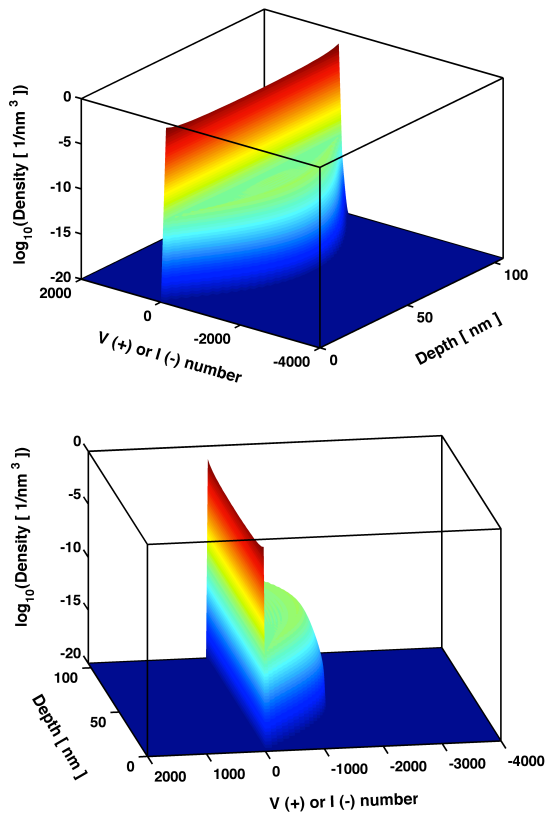

Figure 3. Model calculated volumetric density/concentration of all defect clusters plotted versus cluster c omposition and depth at the fluence of 5×10^{12} ions/cm^2 for a 105 nm thick foil assuming Frenkel pair production mode with only single interstitial ($E_m^I = 0.1$ eV) and single vacancy ($E_m^V = 1.3$ eV) being mobile at a flux of 1.6×10^{11} ions/cm^2/s.

We started our model calculation with $E_m^I = 0.1$ eV and $E_m^V = 1.3$ eV and focused on a 105 nm thick foil and an ion flux of 1.6×10^{11} ions/cm^2/s. Figure 3 illustrates the direct output of all the model calculations in this study, i.e., the volumetric density/concentration of all defect clusters at all depth grids and all doses/fluences. From Fig. 3 it can be seen that interstitials undergo significant clustering while the vacancies do not. This is because the interstitials are highly mobile but the vacancies are essentially immobile at 80°C, and this is consistently observed in the present study as long as a value above ~0.9 eV is used for E_m^V. The output from the model can be easily analyzed to extract the quantities that are measurable/observable in the experiments so that direct comparisons can be drawn between the model and the experiments.

It is important to note that not all the defects in the model, but only those with a diameter exceeding the TEM resolution limit, can be observed in experiments. The resolution limit in such TEM experiments varies slightly with material conditions as well as TEM operating conditions (e.g., plane-view vs. 3D tomography), in the range of 1.3~1.5 nm in the present study.

The areal density of *observable* interstitial loops obtained by applying a resolution limit of 1.5 nm to the model results for the 105 nm thick foil with $E_m^I = 0.1$ eV and $E_m^V = 1.3$ eV is plotted versus nominal dose in Fig. 4 (a). The density increases linearly until the fluence of 3×10^{11} ions/cm^2 after which it shows a tendency to saturate while slowly increasing. By the fluence of 5×10^{12} ions/cm^2 the modeled areal density reaches ~8×10^{-7} /nm^2. There was no experimental data for the 105 nm foil thickness at the same flux. However, the projection from the experimental data for other foil thicknesses at the fluence of 5×10^{12} ions/cm^2 (see Fig. 2) indicates an areal density of a few times 10^{-3} /nm^2 for a 105 nm thick foil, which is higher than the model prediction by four orders of magnitude. The size distribution of observable interstitial loops at the fluence of 5×10^{12} ions/cm^2 analyzed from this set of model results using the same resolution limit of 1.5 nm is shown in Fig. 5 (a). The modeled distribution shows a peak in the 8~8.5 nm size interval. In the experiments, nevertheless, the vast majority of observed loops have sizes less than 4 nm at the same nominal dose and same ion flux for foil thicknesses from 24 nm to 80 nm, and the size distribution shows only slight dependence on the foil thickness. It is thus clear that the model, with the assumed production mode and migration energies, over-predicts the growth of the loops. The under-prediction of loop density and over-prediction of loop growth both seem to suggest that the assumed mobility of interstitials is too high, since higher mobility is expected to enhance all the kinetic processes, including recombination with virtually immobile vacancies, diffusing and sinking to surfaces, and clustering with other interstitials. Thus, one is tempted to think that it is possible to resolve the large discrepancy between the model and the experiments by increasing E_m^I without changing the assumed Frenkel pair production mode.

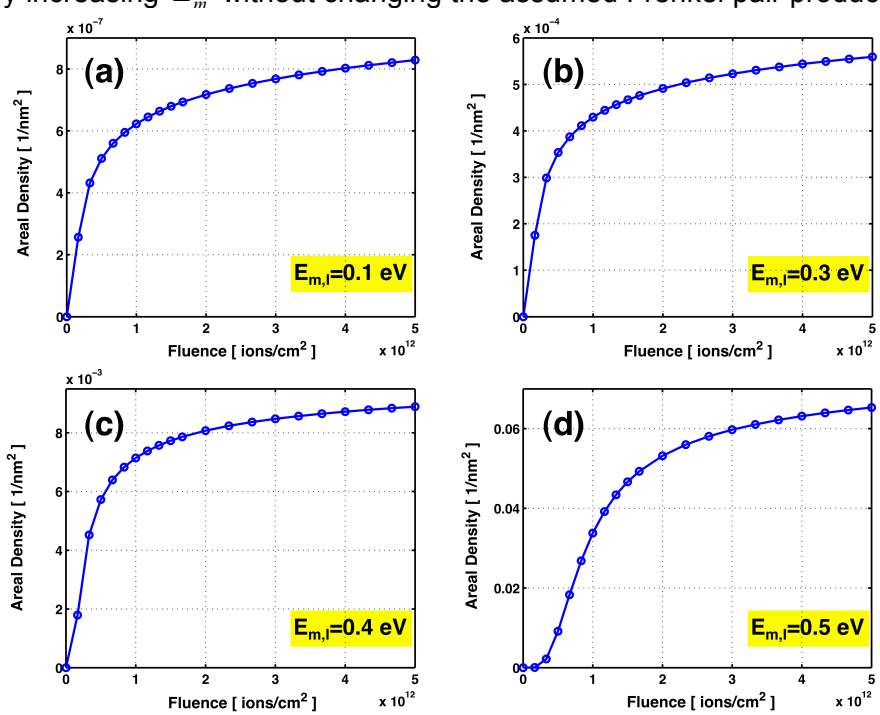

Figure 4. Model-predicted areal density of observable defect clusters (diameter no less than 1.5 nm) as a function of dose for a 105 nm thick foil assuming Frenkel pair production mode with only single interstitial ($E_m^I = 0.1,\ 0.3,\ 0.4, 0.5$ eV) and single vacancy ($E_m^V = 1.3$ eV) mobile at a flux of 1.6×10^{11} ions/cm^2/s.

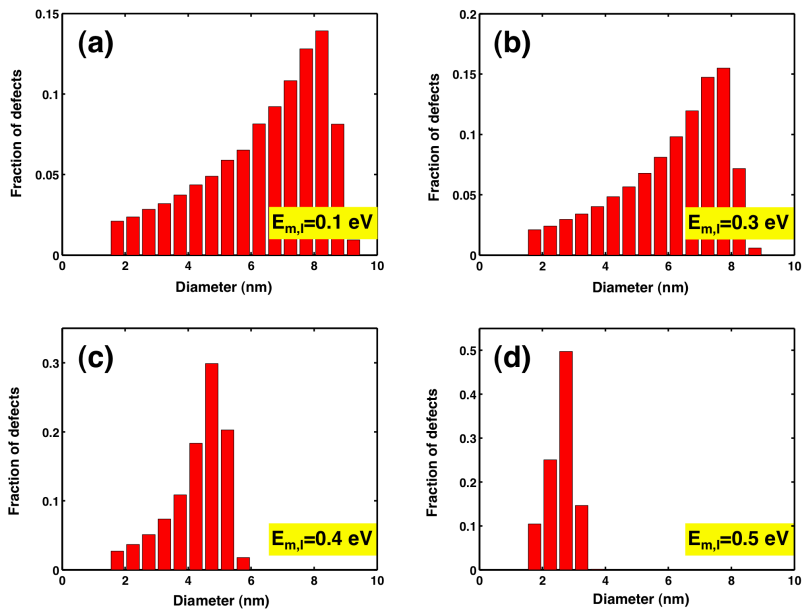

Figure 5. Model-predicted size distribution of observable defect clusters (diameter no less than 1.5 nm) at the fluence of 5×10^{12} ions/cm^2 for a 105 nm thick foil assuming Frenkel pair production mode with only single interstitial ($E_m^I = 0.1,\ 0.3,\ 0.4, 0.5$ eV) and single vacancy ($E_m^V = 1.3$ eV) mobile at a flux of 1.6×10^{11} ions/cm^2/s.

Indeed, as shown in Fig. 4 (b-d), when E_m^I is increased from 0.1 eV to 0.3, 0.4 and 0.5 eV, the model-predicted areal density of observable loops increases by orders of magnitude. With $E_m^I = 0.4$ eV, the model predicts an areal density on the same order of magnitude as observed in the experiments, and with $E_m^I = 0.5$ eV the model predicts an areal density even higher than observed in the experiments by one order of magnitude. Meanwhile, the model-predicted size distribution also shifts to smaller loop sizes with increasing E_m^I, and, in particular, with $E_m^I = 0.5$ eV the model-predicted sizes fall very close to the sizes observed in the experiments. However, the 0.4 or 0.5 eV migration energy of interstitials that has to be used in order to bring the model close to the experiments is apparently too high to be realistic, given that a recovery stage occurs at 33~39 K in Mo following electron irradiation. Therefore, it can be concluded that either the assumption of Frenkel pair production or the assumption of only single interstitial and single vacancy being mobile is incorrect.

Frenkel Pair Production Mode and All Interstitial Loops Mobile

It has been consistently seen in many MD simulations that interstitial loops containing a few to several hundreds of single interstitials in BCC metals are highly mobile with nearly size-independent migration energies close to or even lower than the single interstitial migration energy E_m^I. In BCC iron, for example, MD simulations performed by Marian et al. disclosed a migration energy of I_n that initially decreases but quickly stabilizes with increasing n, following an expression of $E_m(n) = 0.06 + 0.07n^{-1.3}$ (eV), and diffusivity pre-factors expressed as $D_0(n) = 8.98 \times 10^{11} n^{-0.61}$ (nm^2/sec). Quite differently, however, ab initio calculations in BCC iron performed by Fu and Willaime revealed increasing migration energies from single interstitial to di-interstitial cluster, and the ab initio values, 0.34 and 0.42 eV, are very close to the E_m^I determined in earlier resistivity recovery studies in iron. The mobilities of other interstitial clusters containing three or more interstitials were not examined in the ab initio calculations

unfortunately. More recently, in a TEM experimental study Arakawa et al. observed and analyzed the motion of interstitial loops in BCC iron containing thousands of single interstitials, and reported a size-independent migration energy of 1.3 eV for all the observed loops and pre-factors in the form $D_0(n) = (2.3 \pm 0.3) \times 10^{15} n^{-(0.80 \pm 0.02)}$ (nm^2/sec). Arakawa et al. explained this large migration energy value as the result of combined kink formation and impurity dragging mechanisms, and argued that by assuming typical values of impurity migration energies the migration energy of "naked" loops could be deduced to be ~0.4 eV, which is close to the values determined for I and I_2 in ab initio calculations and for I in resistivity recovery experiments.

In Mo, there have not been such intensive studies on the mobilities of interstitial clusters/loops. However, considering the structural similarity of Mo and BCC iron, it is not unlikely that interstitial clusters/loops in Mo also have mobilities, and that their mobilities, particularly for large clusters, are also subject to impurity dragging effect. It is thus interesting to examine how the model results presented in the last subsection may be modified by the cluster/loop mobilities. Table 1 lists the first set of mobility data we chose on an empirical basis for interstitial clusters/loops in Mo by considering the various studies in BCC iron mentioned above. In this set, loops containing more than 7 interstitials are assigned a constant migration energy of 1 eV and pre-factors with a power-law size dependence, whereas the migration energies and pre-factors of small clusters/loops are assigned in a way that gradually connects the single interstitial migration energy and pre-factor to those of large loops $I_{n>7}$.

Fig. 6 (a) and Fig. 7 (a) show the effects of the cluster/loop mobilities, with values listed in Table 1, on the areal density and size distribution, respectively, of observable loops for the 105 nm thick foil at the flux of 1.6×10^{11} ions/cm^2/s with $E_m^I = 0.4$ eV and $E_m^V = 1.3$ eV. By including the cluster/loop mobilities, the areal density saturates faster, at lower doses/fluences, than in the previous case where only single interstitial and single vacancy were considered mobile, and the new saturation value is lower than the previous value by almost three orders of magnitude. The sizes of the most populous loops shift from the bin at 4.5~5.0 nm to the bin at 8.5~9.0 nm, indicating significantly enhanced loop growth. Fig. 6 (b) and Fig. 7 (b) show similar effects of the cluster/loop mobilities with $E_m^I = 0.5$ eV. Although the effects in this case appear not so dramatic as in the case with $E_m^I = 0.4$ eV due to the fact that the different value of E_m^I leads to different migration energies of small clusters I_2~I_7 in the initial mobility set as shown in Table 1, the over one order of magnitude reduction in the saturation areal density by cluster/loop mobility is still significant.

Table 1. Initial set of interstitial cluster/loop mobility data

	$I_{n>7}$	I_7	I_6	I_5	I_4	I_3	I_2	I
D_0 (nm^2/sec)	$10^{12} \times n^{-0.7}$	$10^{12}/7$	$10^{12}/6$	$10^{12}/5$	$10^{12}/4$	$10^{12}/3$	$10^{12}/2$	10^{12}
E_m (eV)	1	E_m^I +0.5	E_m^I +0.35	E_m^I +0.15	E_m^I -0.05	E_m^I -0.05	E_m^I +0.05	E_m^I (varied)

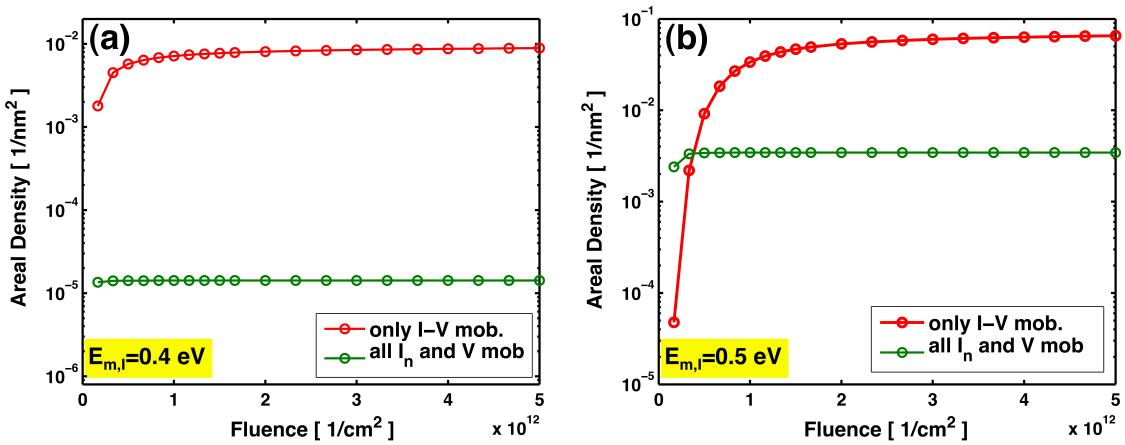

Figure 6. Comparison, for $E_m^I = 0.4,\ 0.5$ eV, of areal density of observable loops (diameter no less than 1.5 nm) predicted by two sets of model calculations for a 105 nm thick foil at a flux of 1.6×10^{11} ions/cm^2/s, both assuming Frenkel pair production mode, but one set considering only single interstitial and single vacancy mobile and the other considering all interstitial clusters/loops (with mobilities listed in Table 1) and single vacancy mobile.

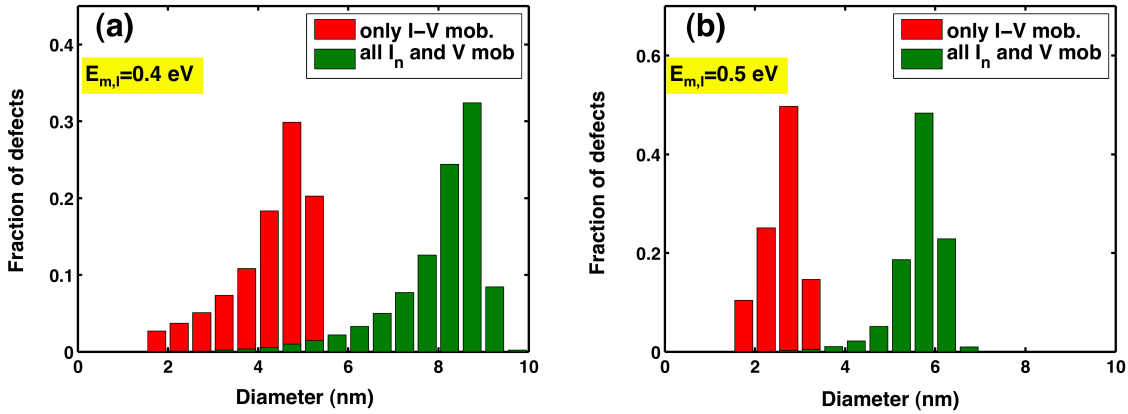

Figure 7. Comparison, for $E_m^I = 0.4,\ 0.5$ eV, of size distribution of observable loops (diameter no less than 1.5 nm) predicted by two sets of model calculations for a 105 nm thick foil at the fluence of 5×10^{12} ions/cm^2 with a flux of 1.6×10^{11} ions/cm^2/s, both assuming Frenkel pair production mode, but one set considering only single interstitial and single vacancy mobile and the other considering all interstitial clusters/loops (with mobilities listed in Table 1) and single vacancy mobile.

These effects of including cluster/loop mobilities can be understood in the same way as the effects of lowering E_m^I in the previous subsection. A case where only single interstitial and single vacancy are considered to be mobile, as in the previous subsection, is equivalent to a case in which the clusters/loops are mobile but with virtually zero mobilities (due to too high migration energies to be thermally activated, for example). From zero to the values listed in Table 1, the mobilities of interstitial clusters/loops are significantly enhanced, which leads to more severe loss of observable loops through capturing vacancies and thus shrinking, and diffusing and sinking to surfaces, while they form larger clusters by capturing single interstitials and other interstitial clusters/loops at a faster pace. Evidently, including the cluster/loop mobilities, regardless of their values chosen to use, can only aggravate rather than resolve the problem of under-predicting the areal density and over-predicting the loop sizes of the model

based on Frenkel pair production assumption with reasonable migration energies of single interstitial and single vacancy.

Intra-cascade Cluster Production Mode and All Interstitial Loops Mobile

SRIM analysis shows that ~30% of all the PKAs induced by 1 MeV Kr^+ in Mo possess kinetic energies above 1 keV. Previous MD simulations on cascades in BCC metals showed that PKAs with a few keV or more kinetic energy can directly produce small interstitial and vacancy clusters rather than Frenkel pairs. There have unfortunately not been such MD studies in Mo, hence in this study we used the intra-cascade cluster production probabilities from MD simulations in BCC iron by Stoller et al. as a first order approximation for Mo with recognition that the true values in Mo may be somewhat different. Introducing the intra-cascade cluster production probabilities to the cases discussed earlier with the same initial set of cluster/loop mobilities as listed in Table 1 resulted in such dramatic increase in the areal density of observable loops and reduction in the cluster sizes that the previous under-prediction of density and over-prediction of size were excessively corrected, even when a low migration energy of 0.1 eV was used for single interstitial. This suggested that the small clusters being produced by cascades might have higher mobilities than those listed in Table 1. Therefore, optimization of the mobility parameters was carried out. Table 2 lists the currently achieved set of mobilities that have produced excellent agreement of the model with the key experimental results as to be shown in the following.

Figures 8-10 compare the areal densities of observable loops obtained in the in-situ experiments with those predicted by the model with intra-cascade cluster production and the optimized mobilities of clusters/loops, in foils of various thicknesses irradiated to various fluences at three ion fluxes, 1.6×10^{11} (Fig. 8), 1.6×10^{10} (Fig. 9) and 1.6×10^{9} (Fig. 10) ions/cm^2/s. Note that these density comparisons are made on the linear scale rather than the logarithmic scale typically used in rate theory modeling. For such close and detailed comparisons, a more realistic resolution limit of 1.3 nm that is slightly lower than the 1.5 nm in the previous subsections was used based on the consideration that the TEM image contrast of a dislocation loop produced by the strain field is always slightly larger than the actual loop size. Further, in the TEM experiments, for a given imaging condition (reflection vector) there were always loops with observable sizes falling out of contrast because of the $g\cdot b = 0$ extinction rule. Based on the detailed Burgers vector analysis, the difference between the resolved areal densities using the fixed g=110 (for all dark field images) and the actual areal densities was estimated to be a factor of 1.9. Therefore, to compare with experimental densities, the model-predicted densities were reduced by the factor of 1.9.

As can be seen in Figs. 8-10, the experiments and the optimized model show the same qualitative trends of the areal density with respect to varying ion fluence, foil thickness and ion flux. Specifically, they both show that the areal density of observable loops increases with increasing ion fluence and foil thickness, that for a fixed foil thickness the areal density tends to saturate as fluence increases, and that for a fixed foil thickness at a given ion fluence the areal density of observable loops is lower when a lower ion flux is used for irradiation.

Figure 8 (a) includes experimental data from two different foils irradiated at the same flux of 1.6×10^{11} ions/cm^2/s. The data from the two foils at a common fluence of 5×10^{12} ions/cm^2 indicate the statistical error/scattering in the experimental results. In view of this scattering and

the linear scale of the comparisons, the model predicted areal densities as displayed in Figs. 8-10 can be regarded in excellent *quantitative* agreement with the experimental measurements.

Table 2. Optimized mobility set for interstitial clusters/loops and single vacancy.

	$I_{n>20}$	$I_{11\sim20}$	$I_{1\sim10}$	V
D_0 (nm^2/sec)	$2\times10^{11}n^{-0.7}$	$2\times10^{11}/n$		2×10^{11}
E_m (eV)	1.1	Linear-space (0.1 to 0.8)	0.1	0.9

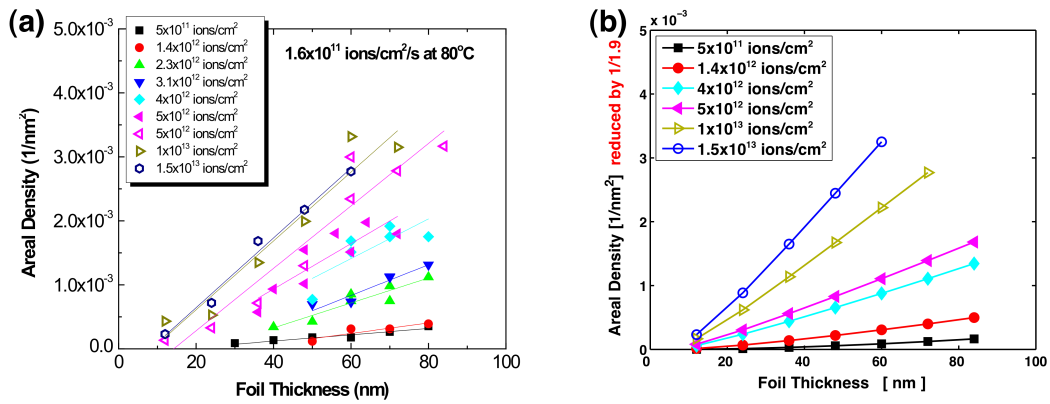

Figure 8. Experimental (a) and model-predicted (b) areal densities of observable loops (diameter no less than 1.3 nm) in foils of various thicknesses irradiated at the ion flux of 1.6×10^{11} ions/cm^2/s to various fluences. The model adopted intra-cascade cluster damage production mode and interstitial clusters/loops mobilities listed in Table 2.

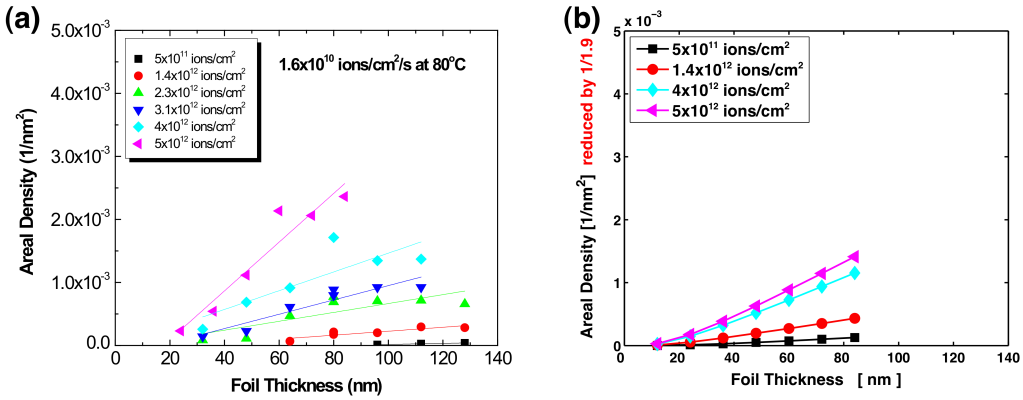

Figure 9. Experimental (a) and model-predicted (b) areal densities of observable loops (diameter no less than 1.3 nm) in foils of various thicknesses irradiated at the ion flux of 1.6×10^{10} ions/cm^2/s to various fluences. The model adopted intra-cascade cluster damage production mode and interstitial clusters/loops mobilities listed in Table 2.

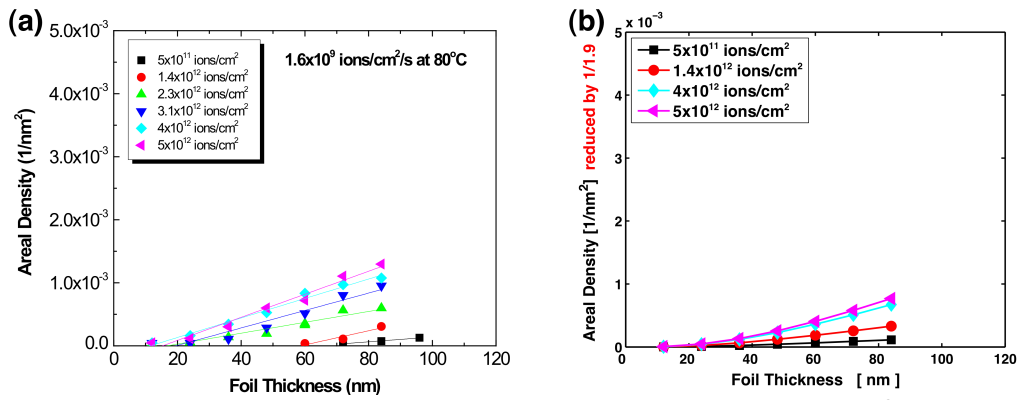

Figure 10. Experimental (a) and model-predicted (b) areal densities of observable loops (diameter no less than 1.3 nm) in foils of various thicknesses irradiated at the ion flux of 1.6×10^{9} ions/cm^2/s to various fluences. The model adopted intra-cascade cluster damage production mode and interstitial clusters/loops mobilities listed in Table 2.

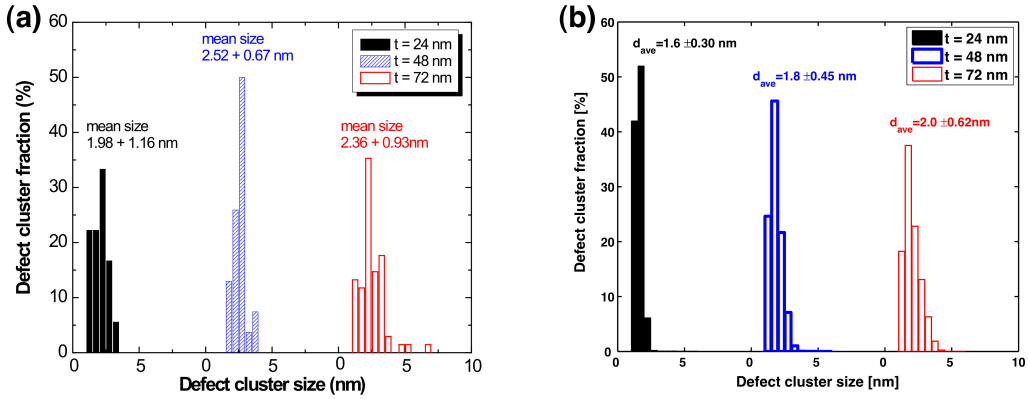

Figure 11. Experimental (a) and model-predicted (b) size distributions of observable loops (diameter no less than 1.3 nm) in foils of various thicknesses irradiated at the ion flux of 1.6×10^{11} ions/cm^2/s to the fluence of 5×10^{12} ions/cm^2. The model adopted intra-cascade cluster damage production mode and interstitial clusters/loops mobilities listed in Table 2.

Further, the size distributions of observable loops obtained in the experiments are compared with those predicted by the optimized model in Figure 11 for foils of three thicknesses, 24, 48, 72 nm, irradiated at the ion flux of 1.6×10^{11} ions/cm^2/s to the fluence of 5×10^{12} ions/cm^2. The model size distributions were obtained with a resolution limit of 1.3 nm, same as for the areal densities in the above. Despite some evident statistical scattering in the experimental size distributions, both the experiments and the model indicate that the size distribution broadens towards larger sizes as the foil thickness increases.

CONCLUSIONS

Nano-scale defect cluster dynamics in thin molybdenum foils under 1 MeV Krypton ion irradiation at 80°C was studied through both in-situ TEM irradiation experiments and coordinated cluster dynamics modeling. The in-situ TEM experiments have provided excellent references for comparing and validating different model assumptions (damage production mode, number of mobile defects/clusters) and for optimizing key kinetic parameters (defect mobilities). The main conclusions of the modeling are: Simple Frenkel pair damage mode with

the assumption of only single interstitial and single vacancy being mobile is unable to account for key experimental observations, namely, defect areal density and size distribution, without introducing unrealistic mobility of single interstitials that significantly contradicts previous resistivity recovery experiments.

Introducing the mobilities of interstitial clusters/loops to the model based on simple Frenkel pair damage mode enlarges the discrepancy between the model and the experiments, regardless of the values chosen for the cluster/loop mobilities.

The model based on intra-cascade cluster production mode, with reasonable parameter optimization, generates excellent agreement with the experiments, both qualitatively and quantitatively, in terms of defect density and size distribution and their dose (fluence), dose rate (flux), and foil thickness dependencies.